Microscopic dynamical description of multinucleon transfer in ^{40}Ar induced peripheral collisions at 15 MeV/nucleon

K. Palli[1], *G. A.* Souliotis[1]*, *T.* Depastas[1], *I.* Dimitropoulos[1], *O.* Fasoula[1], *S.* Koulouris[1], *M.* Veselsky[2], *S. J.* Yennello[3], and *A.* Bonasera[3,4]

[1]Laboratory of Physical Chemistry, Department of Chemistry, National and Kapodistrian University of Athens, Athens, Greece
[2]Institute of Physics, Slovak Academy of Sciences, Bratislava, Slovakia
[3]Cyclotron Institute, Texas A&M University, College Station, Texas, USA
[4]Laboratori Nazionali del Sud, INFN, Catania, Italy

Abstract. This paper deals with heavy-ion peripheral reactions in the Fermi energy region for the production of neutron-rich isotopes. Experimental data of projectile fragments from the reactions of an ^{40}Ar beam at 15 MeV/nucleon with ^{64}Ni and ^{58}Ni targets, collected with the MARS spectrometer at the Cyclotron Institute of Texas A&M University, are considered. Momentum distributions, which provide valuable information on the reaction mechanisms, are extracted and compared with two types of calculations: These are, the Deep Inelastic Transfer (DIT) model and the microscopic Constrained Molecular Dynamics model (CoMD). For the latter, the parameters of the original code were systematically varied in order to achieve an overall satisfactory description of the experimental data. Our results will be discussed.

1 Introduction

The production of neutron-rich isotopes and the path toward the neutron drip line are main subjects for modern nuclear physics research [1–3]. Nuclei far from the beta stability line can provide valuable information on the rapid neutron capture process (r-process), responsible for half of the abundance of heavier than iron nuclei in the universe [4, 5]. Therefore it is essential to explore the reaction mechanisms that produce neutron-rich isotopes. The standard routes to generate neutron-rich nuclides are spallation, fission and projectile fragmentation. Another option leading to products with high neutron excess is for the projectile to capture neutrons from the target [2]. This can take place in multinucleon transfer reactions at energies from the Coulomb barrier to the Fermi energy. In our recent work, we studied reactions below the Fermi energy, since this region combines the advantages of both low- and high-energy reactions. Specifically, the interaction of the projectile with the target leads to fragments with enhanced N/Z ratio, having also high velocities, allowing efficient in-flight collection and separation [6–8].

The present work deals with the distributions of projectile-like fragments from the reaction of an ^{40}Ar beam with ^{64}Ni and ^{58}Ni targets at 15 MeV/nucleon. The experimental data are compared with calculations employing the DIT and the CoMD models followed by GEMINI. Mass and momentum distributions are presented. In section 2, we present an overview of the experimental approach and the data collection. In section 3, we give a brief description of the theoretical models. In section 4, we describe the results of our calculations, followed by our conclusions in section 5.

*e-mail: soulioti@chem.uoa.gr

2 Experimental Set-up and Data

The experimental data on neutron rich nuclide production presented in this work were obtained at the Cyclotron Institute of Texas A&M University and are presented in detail in [9, 10]. In this work we give a brief description of the experimental set-up. An $^{40}Ar^{9+}$ (15 MeV/nucleon) beam, accelerated by the K500 Cyclotron, interacted with ^{64}Ni and ^{58}Ni targets with thickness of 2 mg/cm^2. The MARS recoil separator was used to collect and identify the projectile fragments. The ^{40}Ar beam was sent to the primary target location of MARS with a 4^o angle with respect to the optical axis of the separator and the projectile fragments were collected in the polar angular range of 2.2^o-5.5^o covering a solid angle of $\Delta\Omega$=4 msr. The fragments, after the interaction with the target, traversed a parallel-plate avalanche counter (PPAC), which provided information for the position and the magnetic rigidity, as well as the START-time, and they were focused at the end of the separator passing through a second PPAC (for image-size information and STOP-time) and were collected in a $\Delta E-E$ Si detector telescope. To identify the fragments and obtain their atomic number Z, mass number A, velocity and ionic charge, standard techniques of magnetic rigidity, energy-loss, residual energy and time-of-flight were used on an event-by-event basis [8]. Data were obtained in a

series of successive magnetic rigidity settings of the spectrometer in the range of 1.1-1.5 Tm. We note that this magnetic rigidity range did not fully cover the neutron deficient side of the product distribution which extends down to 0.8 Tm according to our calculations [10]. The proton-rich isotopes with incomplete magnetic rigidity coverage are to the left of the thin solid lines in Fig. 2 and 4.

In fig. 1, we present the experimental data for the momentum distributions for the reaction ^{40}Ar with ^{64} Ni and ^{58}Ni targets at 15 MeV/nucleon that were extracted as part of this work employing the original data [10]. We note that the horizontal axis of the momentum distributions gives momentum per nucleon, which essentially represents velocity. The resolution of the measured P/A was 0.3%. The vertical axis gives the measured differential cross sections with respect to momentum per nucleon, P/A, obtained in the solid angle window of $\Delta\Omega$ = 4 msr at a reaction angle of 4^o as measured with the MARS separator. Each panel represents a different reaction channel. The distributions consist of two peaks, the narrow quasi-elastic peak that corresponds to direct reactions and a wide deep inelastic peak coming from more dissipative collisions.
From the comparison of the momentum distributions for the reactions with the two targets ^{64}Ni and ^{58}Ni, we observe, as expected, lower cross sections for ^{58}Ni, which has a lower N/Z ratio.
We performed binary kinematics calculations and obtained the total excitation energy of the quasi-projectile + quasi-target system. These calculations assume no nucleon evaporation. These excitation energies are reported on some of the peaks of the experimental momentum distributions and help us appreciate the degree of dissipation that is involved. We note that the experimental mass distributions have been obtained and presented in our previous work [10].

3 Description of the Theoretical Models

The theoretical models used to describe the dynamical stage of the collisions were the Deep Inelastic Transfer model (DIT) and the Constrained Molecular Dynamics model (CoMD). Both models follow a Monte-Carlo approach.
The DIT model [11] is a phenomenological model used to describe peripheral collisions. This models considers a di-nuclear configuration of the system allowing stochastic exchange of nucleons, through a "window" that opens in the potential.
We have also used the microscopic model CoMD [12, 13]. This model follows the approach of quantum molecular dynamics [13]. The nucleons are described as Gaussian wavepackets interacting with a Skyrme-type effective interaction with nuclear matter compressibility K=254. The fermionic nature of the system is imposed by a phase-space constraint that enforces the Pauli principle at each time step of the system's evolution. The requirement for the phase space occupation $\bar{f_i}$ is:

$$\bar{f_i} \leq 1 \tag{1}$$

with

$$\bar{f_i} \equiv \sum_j \delta_{\tau_i,\tau_j}\delta_{s_i,s_j}\int_{h^3} f_j(\mathbf{r},\mathbf{p})d^3rd^3p \tag{2}$$

where s_i and τ_i are the z component of the spin and isospin of nucleon i, respectively . The integration is performed in a hypercube of volume h^3 in phase space centered around the point $(\langle r_i\rangle, \langle p_i\rangle)$, in the r and p space, respectively. Within the Gaussian wavepacket representation, it is found necessary to empirically scale the occupation fraction $\bar{f_i}$ as:

$$\bar{f_i} \rightarrow \frac{128}{paulm}\bar{f_i} \tag{3}$$

employing a mass-dependent Pauli constraint parameter, paulm, with the value 94 for the mass range of interest to this work. For each particle i and for each time step, the phase space occupation $\bar{f_i}$ is checked. If the value is greater than 1, an ensemble K_i of nearest particles within distances $3\sigma_r$ and $3\sigma_p$, is determined. Then, for the particles in the ensemble, the momenta are changed in a way that the total momentum is conserved. The ensemble is accepted only if it reduces the value of $\bar{f_i}$. In the present work, the Pauli constraint was enforced further in our calculations, by lowering the value of the parameter paulm from 94 to 87, as will be presented in section 4.

The system is allowed to evolve for time t=600 fm/c (2 zs). The ground state configurations of the nuclei were obtained with a simulated annealing approach. After the annealing, the possible configurations evolve with the model equations of motion and they are accepted if stability is achieved for a time interval of 1000 fm/c. Each configuration, representing initial phase space coordinates of the nucleons, is characterized by a set of model parameters as K, ρ_0, the Pauli constraint parameter ($paulm$) and a set of parameters averaged for each configuration ("achieved parameters"): the binding energy per nucleon $\overline{BE}/A$, the root mean squared radius (R_{rms}), the average $\overline{paulm}$ and the average density $\bar{\rho}$. In the calculations presented in this work, configurations with optimized parameters were employed. In table 1, we present the values of the parameters for ^{40}Ar and ^{64}Ni. In all calculations presented in this work, the value of the surface parameter was set at $C_{sup} = -1$ [12–14].

	$\frac{\overline{BE}}{A}$ (MeV)	σ_r	$paulm$	$\rho_0(fm^{-3})$
^{40}Ar	8.68	1.30	94	0.165
^{64}Ni	8.75	1.30	94	0.165

Table 1. Parameters of optimized configurations for ^{40}Ar and ^{64}Ni with K = 254 MeV.

We note that the experimental values of the binding energy per nucleon of the projectile and target are 8.60 MeV and 8.78 MeV, respectively, very close to the achieved values as reported in table 1.

The de-excitation of the hot projectile-like fragments produced in the dynamical stage was realized by the

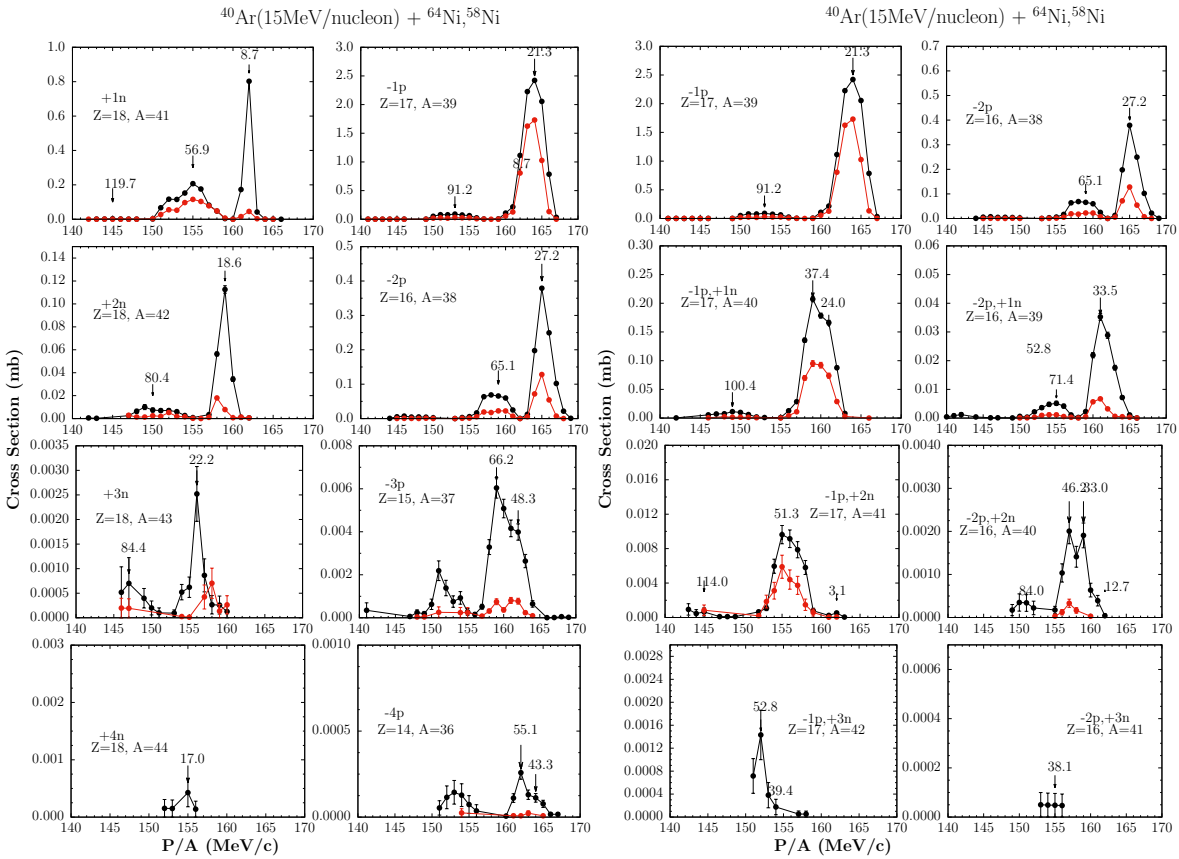

Figure 1. (Color online) Experimental momentum distributions of projectile fragments from the reaction ^{40}Ar (15 MeV/nucleon) with ^{64}Ni, ^{58}Ni. Black points show the data for the reaction with ^{64}Ni target and red points the reaction with ^{58}Ni target.

binary-decay code GEMINI. This statistical de-excitation code [16] uses Monte Carlo techniques and the Hauser-Feshbach formalism to calculate the probabilities for fragment emission with Z < 2. Heavier fragment emission probabilities are calculated via a transition state formalism. Within this model, the final partition of products is generated by a succession of fragment emission in binary decays.

4 Calculations and Comparisons

In this section, we present comparisons of DIT and CoMD calculations with the experimental data. Furthermore, we analyze the effect of some parameters of the CoMD model on the calculations. We chose to focus on a systematic attempt to describe the experimental data with the CoMD model due to its many-body approach, which contains no assumptions on the dynamics, and therefore, provides a microscopically-based description of the process. We present calculations only for the reaction of ^{40}Ar with the neutron-rich target ^{64}Ni, since our goal is to study the production of neutron-rich isotopes. We note that the results with the ^{58}Ni target have similar characteristics as those presented here for the ^{64}Ni target.

4.1 Comparison of the models

For the DIT calculations, after extensive tests and following our previous experience, we scaled the excitation energy of the primary quasi-projectiles to 75% of the original value produced by DIT. For the CoMD calculation we chose to run with the optimized configurations and enhanced Pauli constrained (paulm=87). The effect of the Pauli constraint will be discussed below.

In fig. 2, we present the mass distributions for the reaction ^{40}Ar (15 MeV/nucleon) with ^{64}Ni. The experimental data [10] are shown with the full black points. The region of isotopes to the left of the thin solid lines corresponds to incomplete data coverage as explained in section 2. The vertical dashed green line shows the beginning of neutron pick-up. Each panel represents a specific element. The DIT calculation is shown with the dashed red line and the CoMD calculation with the full green line. By comparing the two calculations, we observe that the DIT model describes reasonably well the neutron rich part of the yield, especially the tails. The CoMD code achieves a rather detailed description of the distributions, however slightly overestimating the n-rich tails.

Regarding the momentum distributions, before comparing the calculations to the experimental data, we had to filter the theoretical distributions for the angular and the momentum acceptance of the experimental setup. We

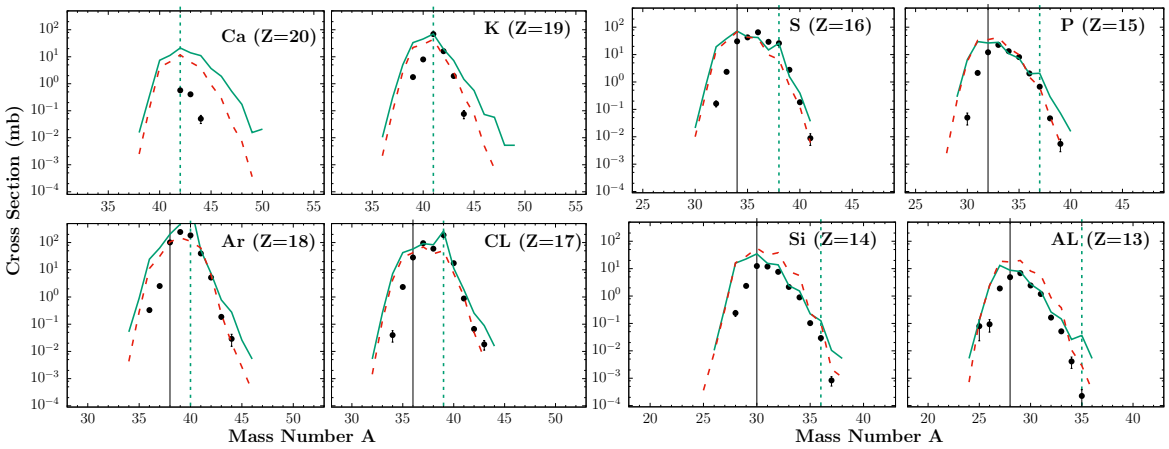

Figure 2. (Color online) Mass distributions of projectile fragments from the reaction of ^{40}Ar (15 MeV/nucleon) with ^{64}Ni. The experimental data are shown by solid black points. The DIT calculation (0.75E*) is shown with the dashed red line and the CoMD calculation (optimum configuration, enhanced Pauli constraint) with the full green line. The region of isotopes to the left of the thin solid lines corresponds to incomplete data coverage. The vertical dashed green line shows the beginning of neutron pick-up.

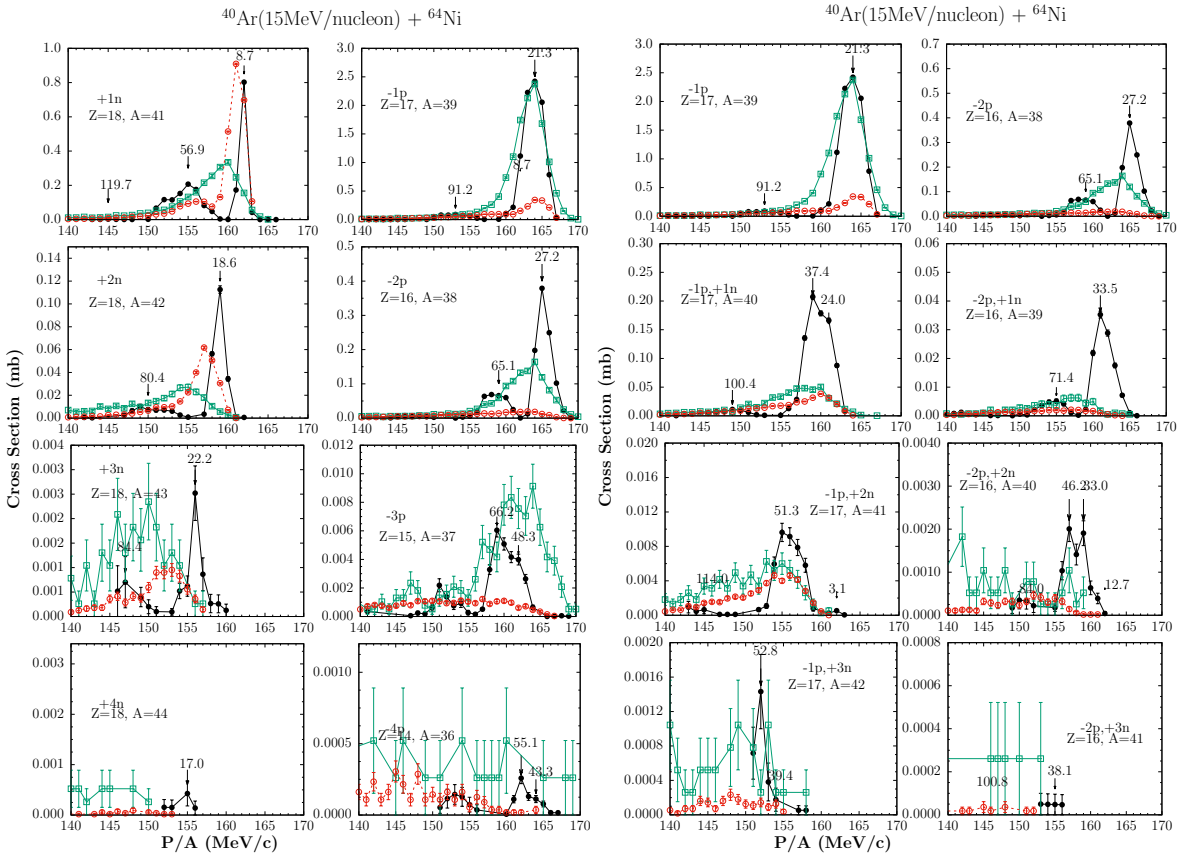

Figure 3. (Color online) Momentum distributions of projectile fragments from the reaction of ^{40}Ar (15 MeV/nucleon) with ^{64}Ni. The experimental data are shown by solid black points. The DIT calculation (0.75E*) is shown with the dashed red line and the CoMD calculation (optimum configuration, enhanced Pauli constraint) with the full green line.

found that this filtering process required the application of a scaling factor of ∼1/20 to the unfiltered calculations, in order to reproduced the experimental acceptance. (The above factor corresponds to the combination of 1/3 and 1/7, respectively, for the polar and azimuthal angular acceptance of the spectrometer.) For the momentum distributions, shown in Fig. 3, the DIT calculations result in low cross sections especially for the proton removal products. The CoMD calculations lead to higher cross sections and wider distributions with respect to the experimental data. It appears that while both models provide a rather reasonable description of the mass distri-

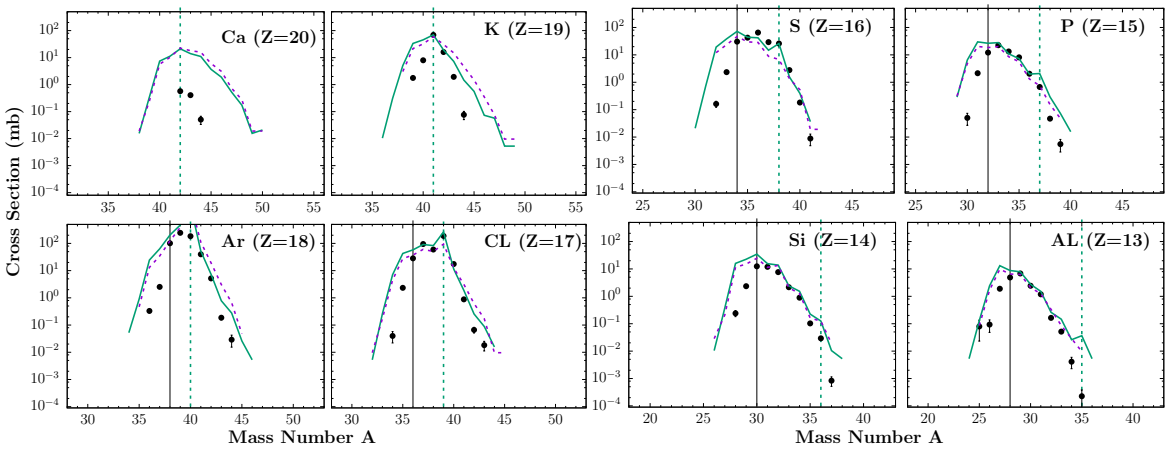

Figure 4. (Color online) Mass distributions of projectile fragments from the reaction of ^{40}Ar (15 MeV/nucleon) with ^{64}Ni. The experimental data are shown by solid black points. The standard CoMD calculation is shown with the dashed purple line and the calculation with enhanced Pauli constraint with the full green line. The region of isotopes to the left of the thin solid lines corresponds to incomplete data coverage. The vertical dashed green line shows the beginning of neutron pick-up.

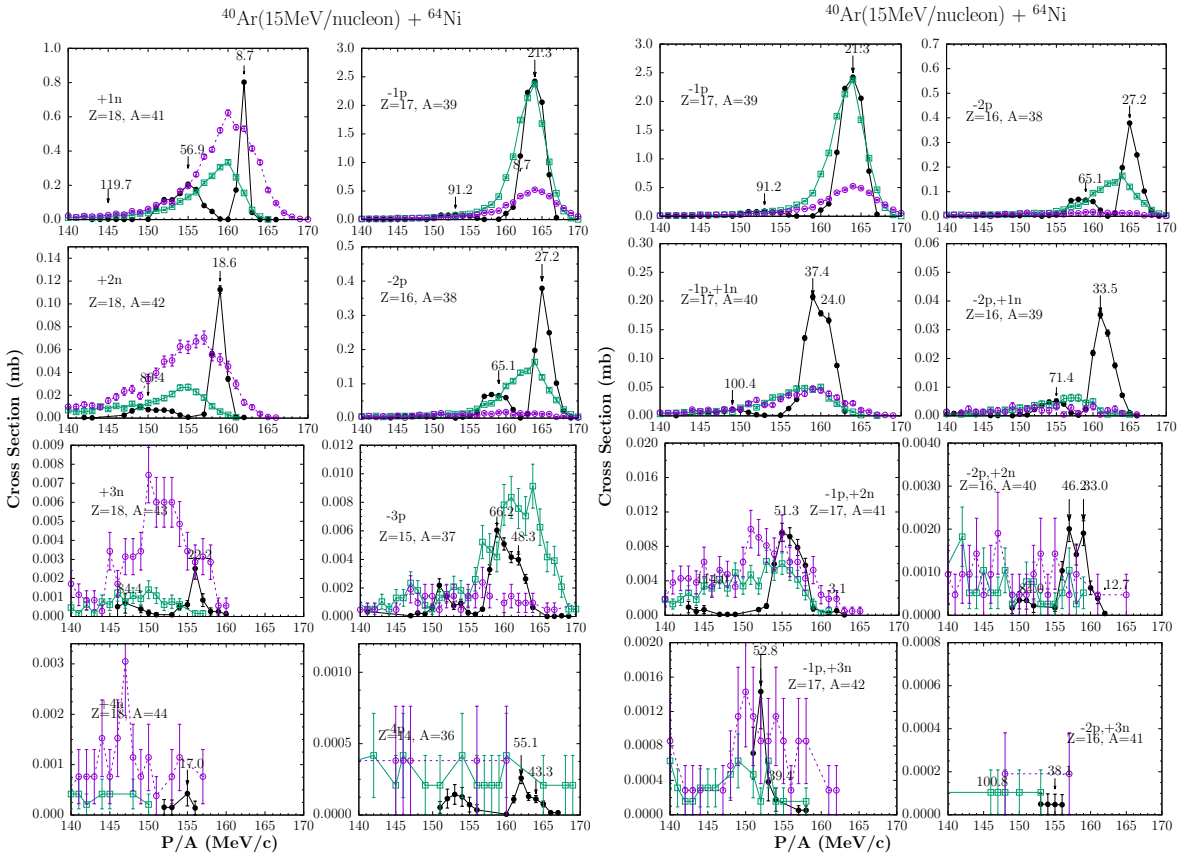

Figure 5. (Color online) Momentum distributions of projectile fragments from the reaction of ^{40}Ar (15 MeV/nucleon) with ^{64}Ni. The experimental data are shown by solid black points. The standard CoMD calculation is shown with the dashed purple line and the calculation with enhanced Pauli constraint with the full green line.

butions, the CoMD model does a better job in describing the experimental momentum distributions in the whole isotope range. Of course, further improvements and tests are necessary.

4.2 Optimization of the CoMD calculations

As already mentioned, in this work we tried to optimize the parametrization of the effective nucleon-nucleon interaction in the CoMD model. The first step was the generation and use of optimized configurations that were discussed in section 3. We applied a more strict enforce-

ment of the Pauli principle by enhancing the Pauli constraint, setting paulm=87, a value lower than the standard value paulm=94 for this mass range (see also table 1). In fig. 4 and 5, we present the effect of this enhancement in the mass and momentum distributions compared with the standard Pauli constraint. With the black points we present the experimental data, with the dashed purple line the standard calculation and with the full green line the calculation with the enhanced Pauli constraint.

The use of enhanced Pauli constraint in the calculations resulted in a rather significant overall improvement. Specifically, for the description of the yields, fig. 4, the calculation with the lower value describes some points of the distribution missed by the calculation with the standard value. For the momentum distributions, fig. 5, we observe better agreement with the data, with higher cross sections for the proton removal products and lower cross sections for the neutron pick-up products. A significant effect on the momentum distributions, is the difference of the width of the peaks, especially in proton removal channels. The calculations with the enhanced Pauli constraint produce narrower peaks, closer to the experimental quasi-elastic peak, compared to the standard calculations. This effect is stronger in the one-proton removal channel. We think that the present calculation with the enhanced Pauli constraint is the best that we have achieved in the context of a systematic variation of CoMD parameters to describe the yields and the momentum distributions of the projectile fragments from the studied reaction.

5 Summary and Conclusions

In continuation of our previous work on the production of neutron-rich nuclides in peripheral collisions below the fermi energy, we studied projectile-like fragments from the reaction an ^{40}Ar beam with ^{64}Ni, ^{58}Ni targets at 15 MeV/nucleon. In this work we obtained and presented the experimental momentum distributions of the ejectiles. Subsequently, we compared both the mass and momentum distributions of projectile fragments from the reaction ^{40}Ar+^{64}Ni with calculations employing the theoretical models DIT and CoMD followed by the deexcitation code GEMINI.

We tried to optimize the parameters of the CoMD model to improve its ability to describe the experimental mass and momentum distributions. We found that the characteristics of the initial configurations used in the CoMD (most importantly, the saturation density and binding energy) are crucial for the outcome of the CoMD calculations. However, within this work, we found that a significant effect comes from an additional enforcement of the Pauli principle. Further exploration and possible improvements of the CoMD model are in line in order to sufficiently describe peripheral reactions with medium-mass heavy ions that lead to neutron-rich products.

6 Acknowledgements

Financial support for this work was provided, in part, by the Special Account for Research Grants of the National and Kapodistrian University of Athens. M.V. was supported by the Czech Science Foundation (GACR) grant No. 21-24281S. SJY and AB were supported by the U.S. Department of Energy under Grant No. DE-FG03-93ER40773 and NNSA Grant No. DENA0003841 (CENTAUR).

References

[1] S. R. Stroberg, J. D. Holt, A. Schwenk, J. Simonis, Phys. Rev. Lett. **126**, 022501 (2021).
[2] G. G. Adamian, N. V. Antonenko, A. Diaz-Torees, S. Heinz, Eur. Phys. J. A **56:47** (2020).
[3] J. Erler, N. Birge, M. Kortelainen, et al, Nature **486**, 509 (2011).
[4] K. Langanke and M. Wiescher, Rep. Prog. Phys. **64**, 1657 (2001).
[5] M. Arnould, S. Goriely, Prog. Part. Nucl. Phys. **112**, 103766 (2020)
[6] G. A. Souliotis, M. Veselsky, G. Chubarian et al, Phys. Lett. B **543**, 163 (2002).
[7] B. Borderie, M.F. Rivet, L. Tassan-Got, Ann. Phys. Fr., 15:4 pp. 287-390 (1990).
[8] G. A. Souliotis, M. Veselsky, S. Galanopoulos, et al., Phys. Rev. C **84**, 064607 (2011).
[9] G. A. Souliotis et al., Progress in Research 2009, Cyclotron Institute, Texas A&M University.
[10] A. Papageorgiou, G. A. Souliotis, K. Tshoo et al., J. of Phys. G **45**, 095105 (2018).
[11] L. Tassan-Got and C. Stephan, Nucl. Phys. A **524**, 121 (1991).
[12] M. Papa, T. Maruyama, A. Bonasera, Phys. Rev. C **64**, 024612 (2001).
[13] M. Papa, G. Giuliani, and A. Bonasera, J. Comput. Phys. **208**, 403 (2005).
[14] N. Vonta, G. A. Souliotis, M. Veselsky, A. Bonasera, Phys Rev. C **92**, 024616 (2015).
[15] A. Bonasera, M. Di Torro, F. Gulminelli, Phys. Rev. C **42**, 3 (1990).
[16] R. J. Charity, M. A. McMahan, G. J. Wozniak et al., Nucl. Phys. A **483**, 371 (1988).
[17] C. A. Bertulani, C. De Conti, Phys. Rev. C **81**, 064603 (2010).
[18] B. Chen, F. Sammarruca, C. A. Bertulani, Phys. Rev. C **87**, 054616 (2013).